

Figure 6. (a) HATPRO microwave radiometer retrieval of air temperature (K) vertical profiles, (b) absolute humidity from HATPRO.

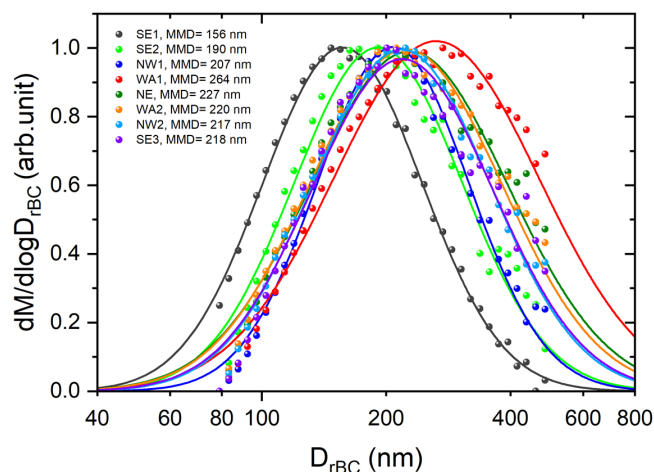


Figure 7. Mass size distribution of refractory black carbon particles estimated during the ATWAICE cruise during distinct airmass conditions. [TS4](#)

and an average of about 1 ng m^{-3} , while Schulz et al. (2019) observed that combustion particles constituted only a minor fraction of the aerosol population in the Canadian Arctic during summer, with near-surface rBC concentrations typically below 2 ng m^{-3} , reflecting weak exchange between the summer polar dome and mid-latitude airmasses. In the present study, most airmass regimes, including NW1, NW2, SE2, SE3, and NE, exhibited similarly low mean rBC concentrations of about $1.4\text{--}1.6 \text{ ng m}^{-3}$, with median values of $0.5\text{--}0.8 \text{ ng m}^{-3}$, indicating that these conditions represent the clean summertime Arctic background (AMAP, 2015; Zanatta et al., 2023; Jurányi et al., 2023). Our observed rBC concentrations are also lower than those reported by Liu et al. (2015) in the European Arctic during spring, where rBC mass concentrations ranged from 20 to 100 ng m^{-3} , as expected from the seasonal transition from the spring Arctic haze period to the comparatively cleaner summer atmosphere. At the same time, the two warm airmass intrusion cases demonstrate that episodic transport can still substantially perturb this otherwise low-rBC environment. These enhanced values are comparable to or approach those reported at Arctic receptor sites such as Pallas, Finland (26 ng m^{-3} ; Raatikainen et al., 2015) and Zeppelin, Svalbard ($39 \pm 23 \text{ ng m}^{-3}$; Zanatta et al., 2018), but remain far lower than those reported for marine and continental regions outside the Arctic, including the remote Atlantic Ocean ($\sim 100 \text{ ng m}^{-3}$) (Pan et al., 2026), south-eastern Arabian Sea ($938 \pm 293 \text{ ng m}^{-3}$), northern Indian Ocean ($546 \pm 80 \text{ ng m}^{-3}$), equatorial Indian Ocean ($206 \pm 114 \text{ ng m}^{-3}$) (Kompalli et al., 2021), Thumba ($670 \pm 571 \text{ ng m}^{-3}$; Nithin et al., 2026), Mukteshwar in the Himalayas ($1000 \pm 600 \text{ ng m}^{-3}$; Raatikainen et al., 2017), and Lulang on the Tibetan Plateau ($310 \pm 550 \text{ ng m}^{-3}$; Wang et al., 2018). The markedly enhanced BC levels during WA1 (eBC as high as 111 ng m^{-3} , rBC as high as 74 ng m^{-3}), while clearly elevated relative to background, remain lower

than the values observed during warm air-mass intrusions in spring (Dada et al., 2022), in subarctic environments, and in near-source high Arctic sites (Popovicheva et al., 2017). Table 1 summarizes our observed M_{rBC} values in comparison with those reported in previous studies from marine, remote, coastal environments.

3.3 Size distribution of refractory BC particles

Figure 7 shows the mass size distributions of rBC particles for the different airmass regimes during the cruise. The size distribution of rBC is relevant for interpreting its atmospheric processing and radiative effects, as the light absorption properties of BC depend on core size, while the observed mass median diameter (MMD) can be influenced by source characteristics as well as by aging and removal during transport (Shiraiwa et al., 2007; McMeeking et al., 2010; Liu et al., 2014; Taylor et al., 2014; Kompalli et al., 2020, 2021; Yang et al., 2025).

The estimated MMD varied substantially across the different transport regimes. During SE1, the MMD was $\sim 156 \text{ nm}$, i.e., the lowest among all regimes in this study. This value lies within the range commonly reported for polluted environments influenced by fossil fuel combustion, although such comparisons should be interpreted cautiously because the observed size distribution at the receptor site reflects not only source emissions but also atmospheric processing during transport (Laborde et al., 2013; Liu et al., 2019; Kompalli et al., 2020; Lim et al., 2023). As the ship moved away from the lower-latitudes towards the central Arctic, the MMD increased progressively; to $\sim 190 \text{ nm}$ during NW1, $\sim 207 \text{ nm}$ during SE2, and $\sim 225 \text{ nm}$ during NE. During NW2 and SE3, the MMD remained similarly larger, at $\sim 217 \text{ nm}$ and $\sim 218 \text{ nm}$, respectively. These observations of MMD indicate a systematic increase in rBC core size from the

Table 1. rBC mass concentration and mass median diameters reported in this study and the values available from previous studies in the marine, remote and coastal environments.

Location/Region	rBC mass concentration (ng m ^{−3})		Mass median diameter (nm)	Reference
	Mean ± SD	Median		
Marine environments				
South easterly 1	48.7 ± 49.8	36.8	156	Present study
North westerly 1	1.4 ± 3	0.6	207	Present study
North westerly 2	1.6 ± 2.5	0.8	217	Present study
South easterly 3	1.6 ± 3	0.8	218	Present study
South easterly 2	1.6 ± 3	0.5	190	Present study
North easterly	1.4 ± 2.7	0.6	227	Present study
Warm airmass intrusion 1	11 ± 14.4	3.4	264	Present study
Warm airmass intrusion 2	5.1 ± 8.3	1.6	220	Present study
Pallas, Finnish Arctic	26		161–231	Raatikainen et al. (2015)
Arctic Ocean	1 ± 1.2		~ 170	Taketani et al. (2016)
Zeppelin, Arctic	39 ± 23		240	Zanatta et al. (2018)
Alert	22 ± 13		160–180	Sharma et al. (2017)
Southern Ocean	0.14			Fossum et al. (2022)
South-eastern Arabian Sea	938 ± 293		190	Kompalli et al. (2021)
Northern Indian Ocean	546 ± 80		200	Kompalli et al. (2021)
Equatorial Indian Ocean	206 ± 114		190	Kompalli et al. (2021)
Remote Atlantic	100		180	Pan et al. (2026)
Remote environments				
Jungfraujoch, Switzerland	13.24	1.4–20.5	220–240	Liu et al. (2010)
Lulang, Tibetan Plateau, China	310 ± 550		160	Wang et al. (2018)
Mukteshwar, the Himalayas, India	1000 ± 600		205	Raatikainen et al. (2017)
North-eastern Qinghai–Tibetan Plateau, China	160 ± 190		187	Wang et al. (2015)
Melpitz	160		140	Yang et al. (2025)
Fukue Island Japan	160 ± 50		200–220	Shiraiwa et al. (2008)
Catalina Island	40 ± 10		153–170	Ko et al. (2020)
Coastal sites				
Thumba	670 ± 571		192	Nithin et al. (2026)
Mace Head	3.31			Fossum et al. (2022)

lower-latitudes towards the central Arctic regimes. However, this gradient should not be interpreted as a unique fingerprint of changing emission sources. In remote regions, rBC size distributions can be modified during transport by size-dependent removal and atmospheric processing, including cloud processing and coagulation (Pan et al., 2026). Therefore, in the absence of independent source-specific tracers and high-resolution chemical composition information, the increase in MMD towards higher latitudes is interpreted here as reflecting the combined effects of distinct sources and atmospheric processing rather than as direct evidence of a transition to a specific source type.

A pronounced enhancement in MMD was observed during the warm airmass intrusion regime WA1, for which the estimated MMD was higher than 260 nm. This value is substantially larger than those observed during the background

central Arctic regimes and coincided with enhanced rBC mass concentrations during the same period. As discussed in Sect. 3.2, WA1 was associated with transport from lower-latitude source regions along with the evidence for biomass burning influence. In contrast, during WA2, the MMD remained close to 220 nm, comparable to the values observed during the central Arctic background conditions. This difference between WA1 and WA2 further indicates that warm airmass intrusions into the central Arctic do not exert a uniform influence on the microphysical characteristics of rBC; rather, their effect on rBC size distribution depends on the transport pathways and the atmospheric processing within the advected airmass.

Changes in MMD during long-range atmospheric transport can arise from multiple competing processes. Size-dependent wet removal may preferentially remove larger BC